

METAL ARTIFACT REDUCTION FOR CT-BASED LUGGAGE SCREENING

Seemeen Karimi, Pamela Cosman

Harry Martz

University of California, San Diego
Dept. of Electrical and Computer Engineering
9500 Gilman Dr., La Jolla, CA 92093-0407

Lawrence Livermore National Laboratories
Center for Nondestructive Testing
7000 East Ave., Livermore, CA 94550

ABSTRACT

In aviation security, checked luggage is screened by computed tomography (CT) scanning, followed by automatic target recognition from the CT images. Metal objects in the bags cause image artifacts that degrade object representation, leading to increased false alarms. We develop a new method, which isolates and reduces artifacts in an intermediate image, based on a numerical optimization that de-emphasizes metal and has a novel constraint for beam hardening and scatter. Results on test bags showed excellent artifact reduction, even for multiple metal objects.

Index Terms— metal artifact reduction, computed tomography, luggage screening, constrained optimization

1. INTRODUCTION

In aviation security, checked luggage is scanned by explosives detection systems (EDS). Many EDS are based on x-ray computed tomography (CT). Automatic target recognition algorithms in these systems analyze the CT images for threats. Metal objects present in the luggage create image artifacts appearing as shadows or streaks. These artifacts misrepresent the surrounding objects, and may lead to apparent splitting of single objects, or the merging of separate objects. Reducing the metal artifacts will likely lead to lower false alarms [1].

Metal artifacts are caused by beam hardening, photon scatter, partial volume effects, photon starvation, and data sampling errors [2, 3]. Beam hardening and scatter cause low-frequency artifacts [2], which are more difficult to remove, while the other sources result in narrow streaks.

Algorithms for metal artifact reduction (MAR) have been developed in medical CT imaging since the 1980s [4]. Despite the advances, there are no widely accepted solutions, and MAR continues to be a challenging research problem. There are three main approaches - sinogram replacement [4–15], energy decomposition with multiple scanning spectra, e.g., [16], and iterative reconstruction (IR) [17–20]. All these methods operate in Radon space (also called projections or sinograms).

Sinogram replacement has been the most explored because of its low complexity. In methods based on sinogram

replacement, a filtered-backprojection (FBP) image is reconstructed from scanner projections, and the metal objects are identified by image segmentation techniques [8, 21]. The projection data corresponding to rays that pass through metal (called traces) are identified by calculation, by forward projection (reprojection) of the metals or even by segmentation in the sinogram. Metal trace data in the sinogram are replaced with an estimate of underlying data, and the corrected sinogram is reconstructed by FBP. It is difficult to estimate the underlying data accurately. Interpolation across the metal traces removes edges from high-contrast structures and renders the projections inconsistent, leading to secondary artifacts. In recent years in medical MAR, image segmentation has been used to identify high-contrast structures, to develop an intermediate image that is called a prior-image [8, 12, 14, 22]. The prior-image is reprojected and thus used to guide data replacement in the scanner sinogram. In luggage, image segmentation cannot separate artifacts from data, because assumptions cannot be made regarding the contents of the images, and because more metal and more artifact interference are present in luggage images.

IR algorithms, such as those based on expectation maximization [23] or algebraic reconstruction technique [24], are used in x-ray CT to reconstruct data with poor signal-to-noise ratio, and where there is missing data [25]. A recent approach is to use IR or numerical optimization for MAR [13, 26, 27] in medical imaging. These algorithms discard all metal trace data. IR and numerical reconstructions usually result in a loss of texture or resolution, so in [13], the optimum solution is used as a prior-image, which is then reprojected, and metal traces from the original sinogram are replaced with the reprojected traces.

In luggage screening, a third or even half the sinogram may contain metal. If all these data are discarded, the reconstructions are poor, as we will demonstrate. Our approach is also hybrid in that it reconstructs a prior-image by optimization, followed by sinogram replacement and FBP. However, we retain the metal projection data with reduced weights, and add a new constraint. Our target prior-image is artifact-free and sparse. The final image has the texture and resolution of FBP reconstruction.

2. METHODS

We first describe a convex optimization problem to construct a prior-image, neglecting any loss of spatial resolution, to explain the objective function and constraint. Then we describe the practical implementation of our complete algorithm.

2.1. Prior-image as a solution of a convex problem

An image in vectorized form is denoted x and the scanner sinogram by b . Let the forward-projection model for log-attenuation projection data be represented by A . Each cell of the matrix A , a_{ij} , contains the fraction of the voxel j that goes into the measured data sample i . For noise-free and artifact free data, the following equation holds:

$$Ax = b. \quad (1)$$

We minimize a regularized weighted least squares (WLS) error as shown in Eqn. (2). In WLS problems, the weights de-emphasize samples (ray-sums) that have higher noise. However, our weights de-emphasize the samples according to the attenuation through metal.

$$\begin{aligned} \min_x (Ax - b)^T W (Ax - b) + \beta \|x\|_{TV} \\ \text{subject to } I_P(Ax - b) \succeq 0. \end{aligned} \quad (2)$$

We first discuss the objective function. The regularization term $\|x\|_{TV}$ is the total variation norm and β is its strength. The total-variation norm has been used for reconstruction from incomplete data [25, 28]. We use it to reward sparsity. The artifact reduction is mainly achieved by the weights and constraint, not regularization. W is a matrix of weights:

$$W = \mathbf{diag}(w(i)) = \exp(-\lambda \sum_{j=1}^V a_{ij} I_1(j)), \quad (3)$$

where V is the number of voxels, and λ is an experimentally determined constant, set to 0.2. In Eqn. (3), I_1 is an indicator function:

$$I_1(j) = \begin{cases} 1 & x(j) > M_1 \\ 0 & \text{otherwise.} \end{cases} \quad (4)$$

The threshold M_1 is set to 4000 modified Hounsfield units (MHU). A voxel above this threshold is interpreted to contain metal or be close to metal. In the MHU scale, water is 1000 MHU and air is zero.

Now we discuss the constraint in Eqn. (2). The symbol \succeq denotes a vector inequality. This constraint is motivated by the knowledge that the low-frequency metal artifacts are due to beam hardening and scattered radiation. Both work in the same direction: the measured attenuation is lower than the ideal (monoenergetic-equivalent) attenuation. I_P is a diagonal matrix containing a second indicator function for metal.

$$I_P = \mathbf{diag}(p(i)) = \begin{cases} 1 & \sum_{j=1}^V a_{ij} I_2(j) > 0 \\ 0 & \text{otherwise} \end{cases} \quad (5)$$

and

$$I_2(j) = \begin{cases} 1 & x(j) > M_2 \\ 0 & \text{otherwise,} \end{cases} \quad (6)$$

where M_2 is set to 10000 MHU. We have used two different metal thresholds. For weighting, $M_1 = 4000$ MHU, and for the constraint $M_2 = 10000$ MHU. This is because we apply the constraint only for high atomic number metals such as copper or iron, for which more beam hardening is expected.

2.2. Practical Implementation

An FBP reconstruction of the scanner sinogram is called the original image, X_{Orig} . We identify metal objects in the original image by region growing.

The prior-image should represent the attenuation of objects dense enough to cause secondary artifacts, such as water and plastics. The convex problem is too large to solve directly. We decrease the size of the problem by solving for a miniature image. The miniature image is reduced by four in each dimension. We low-pass filter and downsample projections by factors of four in views and samples. This reduces reconstruction time by a factor of 16^3 .

The construction of the prior-image is illustrated in Fig. 1. We forward project the metal voxels and calculate the weights with Eqn. (3). Eqn. (2) is solved using the Mosek software (Mosek ApS, Denmark) [29]. Let the optimal solution be denoted X_C^{mini} . X_C^{mini} can be upsampled to the same size as X_{Orig} , and used as the prior-image, but we do not do so because although larger structures are preserved, small structures are degraded. Instead, we reconstruct a second image:

$$X_{LS}^{mini} = \min_x (Ax - b)^T (Ax - b) + \beta_2 \|x\|_{TV}. \quad (7)$$

In Eqn. (7), there are no weights or constraints and $\beta_2 = 0.1\beta$. The difference between X_C^{mini} and X_{LS}^{mini} gives an image consisting mainly of artifacts, X_A^{mini} :

$$X_A^{mini} = X_C^{mini} - X_{LS}^{mini}. \quad (8)$$

We upsample X_A^{mini} using bicubic interpolation to get a full-size artifact image X_A . Artifacts are removed from X_{Orig} by subtracting X_A to give X'_{Prior} (not shown in Figure 1).

$$X'_{Prior} = X_{Orig} - X_A. \quad (9)$$

We copy the segmented metal voxels from X_{Orig} to X'_{Prior} , which gives us more accurate metal traces. Lastly, we clip small CT values (< 500 MHU) to zero to remove small residual artifacts in low density material, and obtain X_{Prior} .

We forward project the prior-image, and use the reprojections to guide the replacement of metal trace data in the scanner sinogram following a previously published method [7]. The corrected sinogram is reconstructed with FBP.

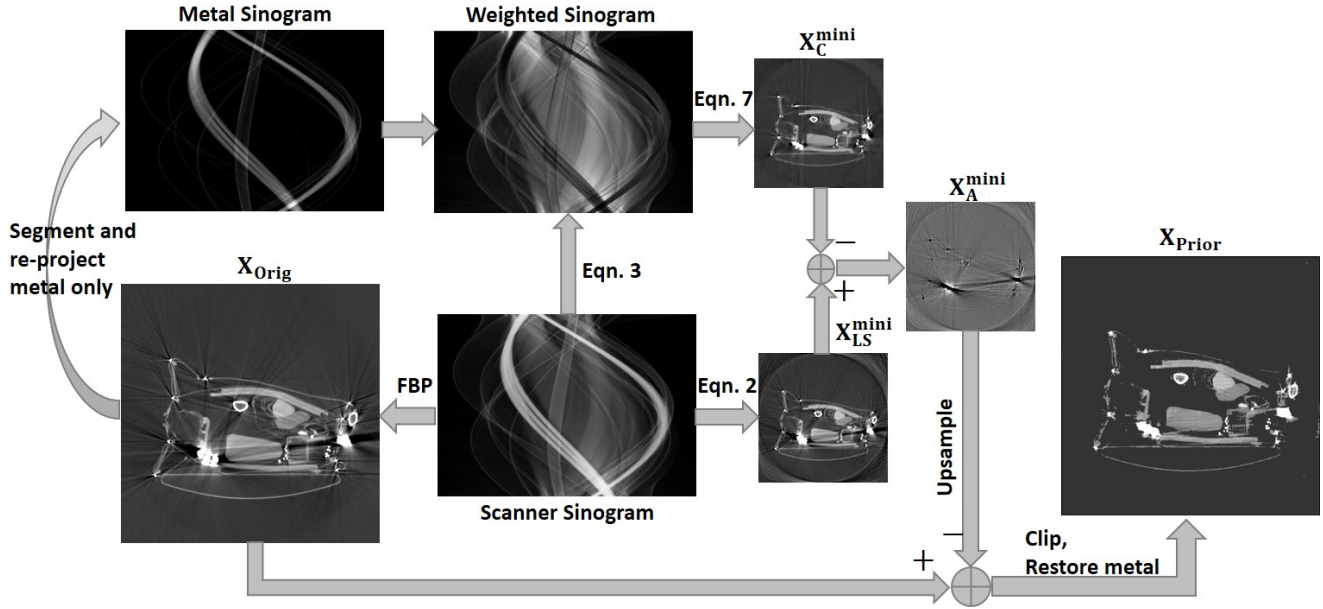


Fig. 1. Pictorial representation of the construction of the prior-image. The flow starts with the scanner sinogram. The optimal solutions to Eqns. (2) and (7) are shown in the smaller images (not to scale).

3. RESULTS

Our data set was supplied by the ALERT group at Northeastern University [30]. Bags were scanned on a medical scanner (Imatron, San Francisco, California) with a tube peak voltage of 130 kV in an axial half-scan mode. The slice thickness is 1.5 mm, the field of view is 475 mm, and image size is 512^2 . There were 864 views / scan, and 888 samples / view.

Fig. 2 shows pairs of original and MAR images. Bright and dark metal artifacts are nearly eliminated. The original images contain artifact amplitudes of a few hundred MHU, which could result in objects wrongly being split or merged by automatic target recognition. The artifacts are nearly eliminated while the structures are preserved, because the prior-image included most of the structures but not the artifacts.

Although there is an overall improvement with MAR, our algorithm has limitations. In image regions close to the metal, some artifacts remain because relevant projections are de-emphasized. There may also be a loss of resolution along the streaks, which is common to most MAR algorithms [31]. During data replacement, interpolation across metal traces blurs edges along the rays unless they were perfectly captured in the prior-image. Edges from relatively less dense materials may not be preserved in the prior-image.

We compare our method against the iterative projection replacement method (IPR) [13]. We chose this benchmark because of its good results on medical images, and because it makes no application-specific assumptions. We computed IPR prior-images of the same size as ours. This made it possible to reconstruct the images on our 16-processor GPU with

96 GB RAM using the same solver, NESTA, [32] and optimization problem definition. While the authors do not specify image sizes in [13], they state that resolution matching is not required. An IPR image is shown in Figure 3. Objects appear blurred together because too much sinogram data has been discarded. We also compare with the most commonly used benchmark in MAR literature [5], also shown in Figure 3. This image has secondary artifacts and loss of detail.

4. CONCLUSIONS

We have developed a new metal artifact reduction method for luggage screening. Results show significant artifact reduction. Our contributions are in three areas. 1. We have a new formulation of an optimization problem, including projection weighting and a constraint for beam hardening and scatter. Details and contrast are better preserved with our weighting and constraints. 2. We express our problem as the difference of solutions to two optimization problems, which removes the effects of mismatched spatial resolution from FBP and optimal solutions, and isolates artifacts. 3. Miniaturization allows us to directly solve the optimization problems.

5. ACKNOWLEDGMENTS

This work was supported by Lawrence Livermore National Laboratories and the Science and Technology Directorate of the Dept. of Homeland Security. Scanner data were supplied by the ALERT group. The authors thank Dr. P. Jin for forward projection software and Dr. X. Jiang for a helpful review.

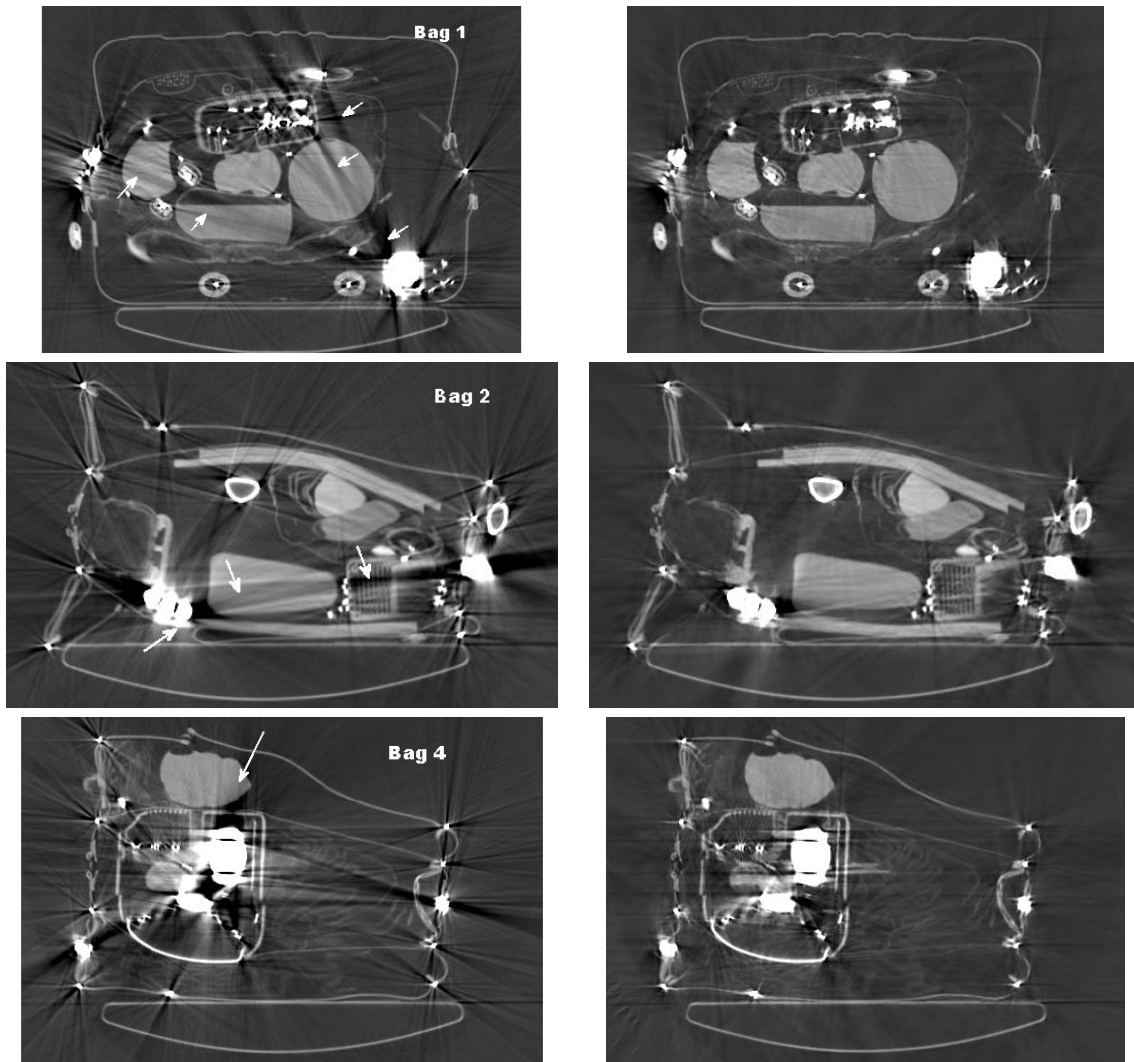


Fig. 2. Example results from our method. The left column shows original images, and the right column shows images with MAR. The arrows point out some artifacts. Window width (WW) = 2500, window-level (WL)=750 MHU. In Bag 1, streaks are present in the original image but reduced in the MAR image. In Bag 2, the object with fine detail on the right hand side of the suitcase appears split, but is restored after MAR. Bag 3 has a large amount of metal inside a boom-box and outside, and a uniform object at the top of the bag. The dark shading in the original image is reduced in the MAR image.

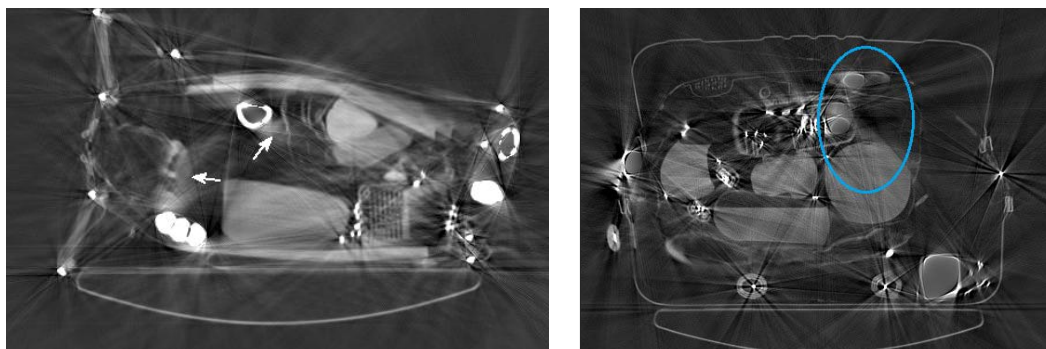


Fig. 3. Images reconstructed with other MAR algorithms. The left image was reconstructed by optimization discarding metal data [13] and the right image had sinogram interpolation without a prior [5]. These images show a loss of detail compared to the MAR images in Figure 2.

6. REFERENCES

- [1] "Final Report on Algorithm Development for Security Applications," in *Algorithm Development for Security Applications* (M. Silevitch, C. Crawford, and H. Martz, eds.), (Boston), 2009.
- [2] A. Kak and M. Slaney, *Principles of computerized tomographic imaging*. Philadelphia, PA 19104: SIAM, 1988.
- [3] B. D. Man and J. Nuyts, "Metal streak artifacts in X-ray computed tomography: a simulation study," in *Nuclear Science Symposium*, pp. 1860–1865, 1998.
- [4] G. Glover and N. Pelc, "An algorithm for the reduction of metal clip artifacts in CT reconstructions," *Medical Physics*, vol. 8, pp. 799–807, 1981.
- [5] W. Kalender, R. Hebel, and J. Ebersberger, "Reduction of CT artifacts caused by metallic implants.," *Radiology*, 1987.
- [6] S. Zhao, D. D. Robertson, G. Wang, B. Whiting, and K. T. Bae, "X-ray CT metal artifact reduction using wavelets: an application for imaging total hip prostheses.," *IEEE Transactions on Medical Imaging*, vol. 19, pp. 1238–47, Dec. 2000.
- [7] R. Naidu, I. Bechwati, S. Karimi, S. Simanovsky, and C. Crawford, "Method of and system for reducing metal artifacts in images generated by x-ray scanning devices," 2004.
- [8] M. Bal and L. Spies, "Metal artifact reduction in CT using tissue-class modeling and adaptive prefiltering," *Medical Physics*, vol. 33, pp. 2852–2859, July 2006.
- [9] H. Li, L. Yu, X. Liu, J. G. Fletcher, and C. H. McCollough, "Metal artifact suppression from reformatted projections in multislice helical CT using dual-front active contours," *Medical Physics*, vol. 37, p. 5155, Sept. 2010.
- [10] C. Golden, S. R. Mazin, F. E. Boas, G. Tye, P. Ghanouni, G. Gold, M. Sofilos, and N. J. Pelc, "A comparison of four algorithms for metal artifact reduction in CT imaging," in *SPIE Medical Imaging* (N. J. Pelc, E. Samei, and R. M. Nishikawa, eds.), p. 79612Y, International Society for Optics and Photonics, Mar. 2011.
- [11] E. Meyer, R. Raupach, M. Lell, B. Schmidt, and M. Kachelrieß, "Frequency split metal artifact reduction (FSMAR) in computed tomography.," *Medical Physics*, vol. 39, pp. 1904–16, Apr. 2012.
- [12] F. E. Boas and D. Fleischmann, "Evaluation of two iterative techniques for reducing metal artifacts in computed tomography.," *Radiology*, vol. 259, pp. 894–902, June 2011.
- [13] J. M. Verburg and J. Seco, "CT metal artifact reduction method correcting for beam hardening and missing projections.," *Physics in Medicine and Biology*, vol. 57, pp. 2803–18, May 2012.
- [14] T. Koehler, B. Brendel, and K. Brown, "A New Method for Metal Artifact Reduction in CT," in *The International Conference in X-ray Computed Tomography*, (Salt Lake City, Utah, USA), 2011.
- [15] C. Glide-Hurst, D. Chen, H. Zhong, and I. Chetty, "Changes realized from extended bit-depth and metal artifact reduction in CT," *Medical Physics*, vol. 40, p. 061711, 2013.
- [16] C. Zhou, Y. Zhao, S. Luo, H. Shi, and L. Zheng, "Monoenergetic imaging of dual-energy CT reduces artifacts from implanted metal orthopedic devices in patients with fractures," *Academic Radiology*, vol. 18, pp. 1252–1257, 2011.
- [17] B. De Man, J. Nuyts, P. Dupont, G. Marchal, and P. Suetens, "An iterative maximum-likelihood polychromatic algorithm for CT.," *IEEE Transactions on Medical Imaging*, vol. 20, pp. 999–1008, Oct. 2001.
- [18] M. Oehler and T. Buzug, "Modified MLEM algorithm for artifact suppression in CT," in *Nuclear Science Symposium Conference Record*, vol. 6, (San Diego, CA), pp. 3511–3518, 2006.
- [19] C. Lemmens, D. Faul, and J. Nuyts, "Suppression of metal artifacts in CT using a reconstruction procedure that combines MAP and projection completion," *IEEE Transactions on Medical Imaging*, vol. 28, no. 2, pp. 250–260, 2009.
- [20] T. Sakimoto and K. Nishino, "Metal artifact reduction in tomosynthesis by metal extraction and ordered subset-expectation maximization (OS-EM) reconstruction," in *SPIE Medical Imaging*, p. 86685M, 2013.
- [21] M. Stille, B. Kratz, J. Müller, N. Maass, I. Schasiepen, M. Elter, I. Weyers, and T. M. Buzug, "Influence of metal segmentation on the quality of metal artifact reduction methods," in *SPIE Medical Imaging* (R. M. Nishikawa and B. R. Whiting, eds.), pp. 86683C–86683C–6, International Society for Optics and Photonics, Mar. 2013.
- [22] S. Karimi, P. Cosman, C. Wald, and H. Martz, "Segmentation of artifacts and anatomy in CT metal artifact reduction," *Medical Physics*, vol. 39, pp. 5857–5868, 2012.
- [23] K. Lange and R. Carson, "EM reconstruction algorithms for emission and transmission tomography," *J. Comput. Assist. Tomogr*, vol. 8, pp. 306–316, 1984.
- [24] R. Gordon, R. Bender, and G. Herman, "Algebraic reconstruction techniques (ART) for three-dimensional electron microscopy and X-ray photography," *Journal of Theoretical Biology*, vol. 29, pp. 471–481, 1970.
- [25] E. Y. Sidky and X. Pan, "Image reconstruction in circular cone-beam computed tomography by constrained, total-variation minimization.," *Physics in Medicine and Biology*, vol. 53, pp. 4777–807, Sept. 2008.
- [26] X. Zhang, J. Wang, and L. Xing, "Metal artifact reduction in x-ray computed tomography (CT) by constrained optimization," *Medical Physics*, vol. 38, no. 2, p. 701, 2011.
- [27] Y. Zhang, H. Yan, X. Jia, J. Yang, S. Jiang, and X. Mou, "A hybrid metal artifact reduction algorithm for x-ray CT," *Medical Physics*, vol. 40, p. 041910, 2013.
- [28] G.-H. Chen, J. Tang, and S. Leng, "Prior image constrained compressed sensing (PICCS): A method to accurately reconstruct dynamic CT images from highly undersampled projection data sets," *Medical Physics*, vol. 35, p. 660, Jan. 2008.
- [29] E. Anderson and K. Anderson, "The MOSEK interior point optimizer for linear programming: an implementation of the homogeneous algorithm," 2013.
- [30] C. Crawford and S. Song, "Scanning Requirement Specification for the ALERT Reconstruction Initiative (Task Order 3)," tech. rep., Awareness and Localization of Explosives-Related Threats (ALERT), 2013.
- [31] A. Mouton and N. Megherbi, "An experimental survey of metal artefact reduction in computed tomography," *Journal of X-ray Science and Technology*, vol. 21, no. 2, pp. 193–226, 2013.
- [32] S. Becker, J. Er, and E. J. C. Es, "Nesta: a fast and accurate first-order method for sparse recovery ," Tech. Rep. 3, California Institute of Technology, 2009.